The landslide stage of the Hsiaolin catastrophe: Simulation and validation

C. Y. Kuo,[1] Y. C. Tai,[2] C. C. Chen,[3] K. J. Chang,[4] A. Y. Siau,[1,4] J. J. Dong,[5] R. H. Han,[6] T. Shimamoto,[7] and C. T. Lee[5]

Received 11 November 2010; revised 1 July 2011; accepted 22 July 2011; published 20 October 2011.

[1] Typhoon Morakot struck southern Taiwan in the summer of 2009, causing the most severe flooding since the 1950s. In the early morning of August 9, rainfall triggered the Hsiaolin landslide, and the resulting debris avalanche covered the township of Hsiaolin Village, Kaohsiung. Around five hundred people were buried alive. Reconstruction of the runout of the debris avalanche would increase understanding of the large-scale avalanches for future hazard mitigation purposes. Simulation of the debris avalanche runout can provide valuable information for this purpose. A new continuum shallow-water model is applied to flow over general topography. The Coulomb friction law is adopted; the friction coefficient is initially determined by high pressure rotary-shearing tests and subsequently fine-tuned by an iterative procedure to minimize the difference between the simulation and the measurement. The friction coefficients measured by laboratory tests are found to be in reasonable agreement with the best-fit result of the simulation. In addition, Voellmy rheology is applied, but it is found that the role of the fluid viscous drag is insignificant. The simulation result in the village area is further corroborated by near-surface magnetic surveys. These indicate that the northern part of the village is dislocated, while the artifact structures of the southern part are buried near their original locations. By comparing the landslide front and the flow direction of the simulation, we are able to confirm, as also described by survivors, that the landslide swept the northern part of the village into the Cishan River, while the southern part was flooded subsequently by the debris from a dam breach about 20 min after the landslide.

Citation: Kuo, C. Y., Y. C. Tai, C. C. Chen, K. J. Chang, A. Y. Siau, J. J. Dong, R. H. Han, T. Shimamoto, and C. T. Lee (2011), The landslide stage of the Hsiaolin catastrophe: Simulation and validation, *J. Geophys. Res.*, *116*, F04007, doi:10.1029/2010JF001921.

1. Introduction

[2] In recent years, Taiwan has witnessed several occurrences of extreme weather conditions. Typhoon Morakot, as an example of precipitation extremes, released more than 2,000 mm of rain on southern Taiwan within three days beginning 7 August 2009 [*Dong et al.*, 2011]. This rainfall almost equals the annual precipitation average in Taiwan. According to the National Disaster Prevention and Protection Commission in Taiwan, the resultant flooding caused 724 deaths. Of these, 474 were in a landslide and debris-flow event in Hsiaolin (the official translation. Several other spellings of the village name (Shiaolin, Siaolin, Xiaolin) are seen in the literature because of different translation schemes.) Village, Kaohsiung. This catastrophe had a severe socio-cultural impact on three Taiwanese aboriginal tribes of the Pingpu group.

[3] From routine aerial photographs and the immediate response of the Agricultural and Forestry Aerial Survey Institute of Taiwan, digital terrain models (DTMs) were generated at a 5-meter resolution for the Hsiaolin landslide. The geological settings are summarized in Figure 1 and by *Tsou et al.* [2011] and *Dong et al.* [2011]. According to the DTMs and the field survey, the major landslide body had an extent of 57×10^4 m^2 (cool colors in Figure 1a) and was estimated to have a volume (the precision is justified based on the precision of the pre/post-event DTMs; see section 4) about 24 ± 2 million m^3, distributed at an average depth of 42 ± 3 m. The landslide moved in the westward direction

[1]Research Center for Applied Sciences, Academia Sinica, Taipei, Taiwan.
[2]Department of Hydraulic and Ocean Engineering, National Cheng Kung University, Tainan, Taiwan.
[3]Graduate Institute of Geophysics and Department of Earth Sciences, National Central University, Jhongli, Taiwan.
[4]Department of Civil Engineering, National Taipei University of Technology, Taipei, Taiwan.
[5]Graduate Institute of Applied Geology, National Central University, Jhongli, Taiwan.
[6]Geologic Environment Division, Korea Institute of Geoscience and Mineral Resources, Daejeon, South Korea.
[7]State Key Laboratory of Earthquake Dynamics, Institute of Geology, China Earthquake Administration, Beijing, China.

0148-0227/11/2010JF001921

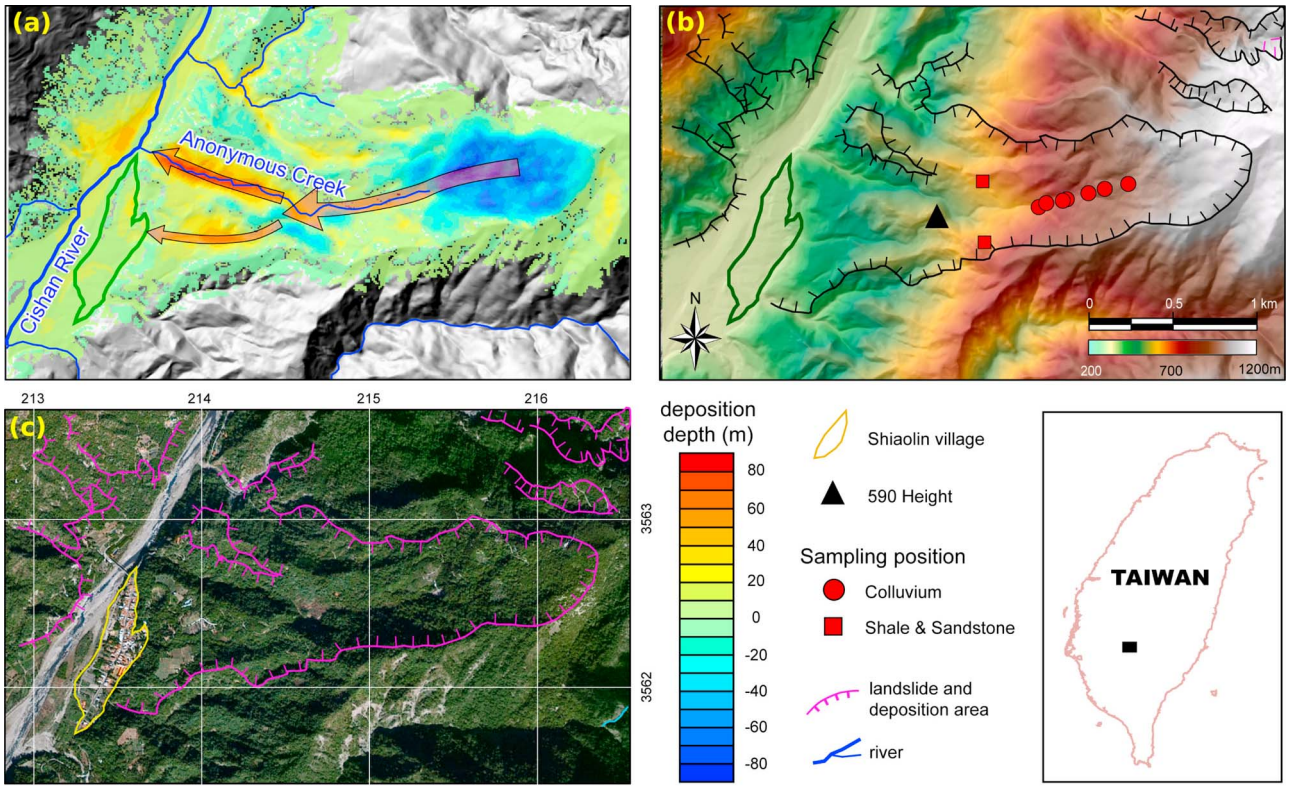

Figure 1. The Hsiaolin area and the geological settings. (a) Aerial photo before the catastrophic landslide superimposed with the elevation differences between the two versions of the digital terrain models (before and after Typhoon Morakot and the block dam breach. Both were taken in 2009). Negative deposit depth (cold colors) represents the scar area. The main deposit is in the Anonymous Creek Valley and the Cishan River channel. The arrows indicate the main runout paths. (b) The elevation of the landslide area. The solid red circles and squares are the sampling locations for colluvium and shale. The large solid black triangle marks the 590 Height, a ridge at an elevation 590 m above the sea level. (c) A birds-eye view of the landscape before the landslide and Hsiaolin village. The Cishan River flows from NE to SW. The horizontal coordinates follow the TWD97 (Taiwan Datum 97) standard system.

as indicated by the thick hollow arrows in Figure 1a. The landslide flow was divided into two streams at about the middle of the runout. It was because there had been a small ridge at 590 m above sea level (marked by the solid black triangle in Figure 1b) and two valleys extended from the west side of the ridge. This ridge is referred as the 590 Height hereafter. The 590 Height had a volume about 1.5 ± 0.2 million m^3 which was removed by the landslide.

[4] The two debris streams, after interacting with the 590 Height, flowed along the two valleys and about a third of the sliding mass further flowed into Cishan River, running from NE to SW. The debris in the Cishan river formed a short-lived block dam and a dam breach occurred about 20 minutes after the landslide which removed most of the deposit in the river channel except a minor portion of 5 ± 1 million m^3. The remaining deposit, mainly in the two valleys to the river, formed the main deposit area (warm colors in Figure 1a). The deposit materials mainly composed of fine particles and fragmented shale blocks with sizes up to a few meters [*Dong et al.*, 2011]. No substantial erosion was found in the exposed runout (mainly between the scar area and the 590 Height), and, therefore, the erosion mechanism was not considered. The total combined volume in the main deposit area was 13 ± 2 million m^3 and the average basal inclination angle was about 15° (±12°, averaging over the slopes by the valleys). The northern valley of the two valleys is now referred as the Anonymous Creek Valley in the present paper and the deposit was in the SWW-NEE direction. The southern valley is referred as the Hsiaolin Slope which was much smoother than the Anonymous Creek Valley. It was this Hsiolin Slope that directed the landslide flow into the Hsiaolin Village. If a loose-measure volume of the sliding body is assumed to have expanded 10%, the flushed materials by the dam breach was estimated about 11 ± 2 million m^3. After the landslide and the dam breach, the village (blocked by the thick green line in Figure 1a) was completely buried.

[5] Reconstruction of the runout path due to the debris avalanche event is fundamental to understanding the complex mass movement process. For this purpose, we adopt a continuum model, similar to shallow water equations, to simulate the landslide. One of the important issues in the model is to include the topographic effect which interacted significantly with the landslide mass in this Hsiaolin event. For example, the topographic effect can be seen from the diversion of the landslide flow into the Anonymous Creek Valley and Hsiaolin Village after the slip mass interacted with the 590 Height and the surrounding ridges. Taking the

topographic effects into the shallow water system is not trivial, mainly because of the complexity of the terrain geometry. *Savage and Hutter* [1991] derived the (1D) model equations in the terrain-fitted curvilinear coordinates. *Gray et al.* [1999] and *Wieland et al.* [1999] extended the Savage-Hutter theory to multidimensions in which the curvature effect is included only in the down-slope direction. Alternatively, *Pudasaini and Hutter* [2003] formulated their theory with a curved and twisted coordinate system for a smooth, curved runout path. In the further pursuit of the continuum model for real topography, several distinctive theoretical techniques have been proposed in the past decade: (1) the Lagrangian models [*Greve and Hutter*, 1993; *Koch et al.*, 1994; *Chen and Lee*, 2000; *McDougall and Hungr*, 2004; *Hungr and McDougall*, 2009], (2) the coordinate-based approaches [*Bouchut and Westdickenberg*, 2004; *Tai and Kuo*, 2008; *Luca et al.*, 2009a], and (3) the dynamic-based approaches [*Denlinger and Iverson*, 2004; *Iverson et al.*, 2004].

[6] In section 2, a two-dimensional model was extended from the model proposed by *Tai and Kuo* [2008] and Y. C. Tai et al. (A depth-integrated description of geophysical mass flows over temporally varying topography of small curvature, submitted to *Physics of Fluids*, 2011). The avalanche flow in the model is assumed to be single constituent, incompressible, thin and to have a uniform velocity profile across the depth, flowing on a fixed topographic surface described by a Coulomb or Voellmy friction law. The topographic effect is manifested as the source of the kinetic momentum. The non-oscillatory numerical scheme of *Jiang and Tadmor* [1997] was adopted for numerical calculations. This approach is not rare. It has been widely applied in snow avalanches [see, e.g., *Pudasaini and Hutter*, 2007]. *Gray et al.* [2003] showed that, even with these drastic simplifications, the model can accurately predict the salient physical phenomena–granular shock waves, dead zones, etc.–observed in debris avalanches. Using a similar hydrodynamic model, *Bouchut and Westdickenberg* [2004] and *Kuo et al.* [2009] resolved satisfactorily the kinetic properties of the Tsaoling landslide, Taiwan, 1999. Nevertheless, for the interested readers, extensive efforts have been made to incorporate material constitutive laws and yield criteria into the dynamic models for both two-dimensional [*Iverson and Denlinger*, 2001; *De Toni and Scotton*, 2005; *Luca et al.*, 2009c] and three-dimensional flows [*Crosta et al.*, 2009].

[7] When the Coulomb friction law is applied, the friction coefficient is the only rheological parameter. This enables us to determine this coefficient by straightforward high pressure rotary-shearing tests on field debris samples, as described in section 3.1. Because the slid mass mainly consisted of shale and colluvium, field samples of both kinds were prepared for the tests. They were prepared with a range of water contents suggested by the field samples and sustained under a high normal stress during the tests, which mimicked the *in-situ* stress condition on the basal surface. Subsequently, in section 3.3, an iteration procedure is presented to minimize the difference between the simulation and the post-event topography for fine-tuning the friction coefficient. This process is used to evaluate the applicability of the scaled-down laboratory measurements for the entire motion of landslides. The reasonable agreement is encouraging. To complement the study, the effect of the volume dilation and the Voellmy friction law were also investigated. They were found to be insignificant to the simulation. Finally, the key validation of the continuum model arises from the corroboration with near-surface magnetic surveys over the buried village area, as presented in section 5.

[8] Although the landslide was triggered by excessive rainfall, we did not consider a mixture model in the present simulation. Instead, the focus was on the kinematics of the fast moving mass and its interaction with the runout topography. The constant friction coefficient was determined with the help of laboratory experiments, in which the Coulomb friction coefficient is calculated by the total reacting torque and the applied normal stress. Hence, the effect of pore water pressure was implicitly lumped into the friction coefficient and the single constituent frictional model was adequate for the present purpose. Nevertheless, we need to mention that the pore pressure plays an important role in regulating landslide motion [*Iverson*, 2005], or lowering the friction force through the frictional heating mechanism when landslides are in motion [*Vardoulakis*, 2002a, 2002b; *Chang et al.*, 2005]. For a landslide with a saturated water content, one may need to apply mixture models [*Iverson and Denlinger*, 2001; *Denlinger and Iverson*, 2001; *Pitman and Le*, 2005].

2. Formulation

[9] As aforementioned, several categories of theoretical models have been proposed to simulate landslide motion over real topography. In the Lagrangian model, the discretized fluid elements undergo acceleration and deformation according to the resultant force and the stress state (with constitutive laws) [*Hungr and McDougall*, 2009; *Crosta et al.*, 2009]. The position and physical variables of the discretized elements are calculated in a way similar to particle tracing. The topographic inclination effect is hence automatically incorporated into the element motion via the gravity acceleration. The complexity arises from resolving the distorted fluid elements during simulation. The dynamic-based approach adopts Cartesian coordinates. The vertical acceleration is taken into account through the correction of the vertical normal stress component to cope with landslide flows over steep terrain [*Greve and Hutter*, 1993; *Koch et al.*, 1994; *Denlinger and Iverson*, 2004; *Iverson et al.*, 2004]. The flow profile is presumed to be along the vertical direction. Significant computational advantages are achieved because the gravity wave speed is constant in individual cells.

[10] The present model, on the other hand, is a coordinate-based approach. The model equations are based on the two-dimensional, fixed topography extensions of *Tai and Kuo* [2008] and Tai et al. (submitted manuscript, 2011). They are derived by constructing a terrain-fitted coordinate system in which the flow depth is defined in the direction normal to the basal surface. Along this depthwise direction, the inertial is of a small negligible magnitude which leads to a hydrostatic pressure. Because of the space limitations, only the associated coordinate system and the resultant model equations are summarized here. A fuller derivation is referred to in the mentioned papers and in the auxiliary material.[1] The verification of this model with experiments

[1] Auxiliary materials are available in the HTML. doi:10.1029/2010JF001921.

is referred to by *Tai and Lin* [2008] and the comparison of the model to other alternatives is discussed in section 2.2.

2.1. Terrain-Fitted Coordinates

[11] Flows over a three-dimensional topography were considered. Let $\vec{X} = (X, Y, Z)^T$ be the position vector of $\mathbf{R}^3$ in the Cartesian coordinates. The x- and y-coordinates lie on the horizontal plane and the z-axis points upwards in the vertical direction, opposite to the direction of gravity (see Figure 2). Notation $\mathbf{x} = (x, y)$ is the two-component vertical projection of the basal point (x, y, z) onto the horizontal plane. If the fixed topographic surface is described by $F(x, y, z) = z - b(\mathbf{x}) = 0$, following the notation of *Bouchut and Westdickenberg* [2004] and *Luca et al.* [2009a], its unit normal vector is then given by

$$\vec{n} = (-\mathbf{s}, c)^T = \left(-s_x, -s_y, c\right)^T = \left(-c\partial_x b, -c\partial_y b, c\right)^T, \quad (1)$$

where

$$\mathbf{s} = c\left(\partial_x b, \partial_y b\right)^T \text{ and } c = \left[1 + (\partial_x b)^2 + \left(\partial_y b\right)^2\right]^{-1/2}. \quad (2)$$

In (1) and (2), the convention for vectors is introduced: the lower case with an overhead arrow, $(\vec{\bullet})$, is for a three-component vector, and the boldface lower case is for a two-component subspace vector. The superscript ^{T} stands for the vector/matrix transpose. Notations $\partial_x b$ and $\partial_y b$ are the derivatives of the topographic surface with respect to the horizontal coordinates x and y, and $b(\mathbf{x})$ is assumed to be sufficiently smooth and differentiable.

[12] On the topographic surface, the terrain-fitted curvilinear coordinates $\vec{\xi} = (\xi, \eta, \zeta)^T = (\boldsymbol{\xi}, \zeta)^T \in \mathbf{R}^3$ are defined where the components ξ and η are the tangential coordinates on the terrain surface and ζ lies in the normal (flow-depth) direction. As long as the flow depth in the ζ–direction is locally smaller than the minimum of the two principal radii of the local curvature tensor, there is a uniquely defined coordinate transformation of position vectors between the Cartesian and the terrain-fitted coordinates.

2.2. Depth Integrated Model Equations

[13] As the flows are generally thin over the topographic surface, the governing equations can be simplified by neglecting the depth-wise momentum component and a depth integration procedure. After performing an appropriate dimensional scaling analysis, the physically significant terms are retained in the final governing equations. In the dimensional form, the model equations are

$$\begin{aligned} &\frac{\partial}{\partial t}(J_b\, h) + \nabla_{\boldsymbol{\xi}} \cdot (J_b\, h\, \mathbf{u}^*) = 0, \\ &\frac{\partial}{\partial t}(J_b\, h\, \mathbf{u}) + \nabla_{\boldsymbol{\xi}} \cdot (J_b\, h\, \mathbf{u} \otimes \mathbf{u}^* + \boldsymbol{\beta}^*) = \boldsymbol{\varsigma}_{\boldsymbol{\xi}}, \end{aligned} \quad (3)$$

where h is the flow depth measured in the direction normal to the basal topography, J_b is the Jacobian determinant on the basal surface for the coordinate transformation. Notations $\mathbf{u}$ and $\mathbf{u}^*$ are the flow velocity in the Cartesian coordinates and in the terrain-fitted coordinates.

[14] These equations (3) are the continuity and the momentum equations. With the present simplification of the constitutive relation, the normal stresses are assumed to be hydrostatic and the shear stresses are assumed to be of some order of magnitude smaller than the normal stresses and, hence, are neglected. The matrix $\boldsymbol{\beta}^*$ contains the hydrostatic pressure

$$\beta^* = cg\frac{h^2}{2}\, J_b \nabla_{\boldsymbol{\xi}} \mathbf{x}. \quad (4)$$

The source term $\boldsymbol{\varsigma}_{\boldsymbol{\xi}}$ represents the net driving force, including both the gravity acceleration and the basal friction

$$\boldsymbol{\varsigma}_{\boldsymbol{\xi}} = -J_b N_b \left[\mathbf{s} + \mu \frac{\mathbf{u}}{||\vec{u}||}\right]. \quad (5)$$

The value of N_b is found by integrating the momentum equation along the flow depth direction. The procedure is similar to the shallow-water equations, which yields

$$N_b = cg\, h + c\, h\, \mathbf{u}^* \cdot \left(\nabla_{\boldsymbol{\xi}} \frac{\mathbf{s}}{c}\right)^T \mathbf{u}. \quad (6)$$

This normal pressure consists of two parts: the first term is the hydrostatic pressure and the second represents the centrifugal force due to the local curvature.

[15] The model equations (3) are written for the Cartesian components of the momentum and stresses in the terrain-fitted coordinates. The difference between the present model and the traditional description of governing equations over curvilinear coordinates is that the new model avoids the calculation of the Christoffel symbols; see for comparison *Luca et al.* [2009a, 2009b]. This form is not the first seen in the literature, but it is a special form (the Eulerian description limit) of the Unified Coordinate (UC) formulism [*Hui and Koudriakov*, 2002; *Hui*, 2007]. As a fuller example, *Tai and Kuo* [2008] and Tai et al. (submitted manuscript, 2011) further elaborate on the capability of moving coordinates in the UC method for their two-dimensional model with erosion and deposition.

[16] A straightforward comparison to the other similar model (BW) proposed by *Bouchut and Westdickenberg* [2004] can be made. The main difference is that in BW, the contravariant velocity is used as the model unknown and the spatial operator is operated in the Cartesian coordinates. Although the BW model has the benefit of a direct integration with the GIS models, the model equations involve the physical variables and flux terms that are coupled with topographic factors. These coupling variables make the physical interpretations somewhat indirect. The present model, on the other hand, uses the Cartesian velocity and the conservation laws are satisfied in the terrain-fitted coordinates. As a result, no special treatments for the numerical implementation of the conservative laws and for the coordinate transformation of the physical quantities is needed.

[17] The resultant model equations comprise a nonlinear balance system that is in conservation form. This system allows sudden changes, i.e., discontinuities or weak solutions of velocity and thickness [*Rericha et al.*, 2002; *Gray et al.*, 2003]. Hence, to solve the equations, a numerical method that can resolve the weak solutions has to be applied. A Godunov-type high resolution non-oscillatory central (NOC) scheme with a total variation diminishing (TVD) slope limiter for the second order accuracy was used

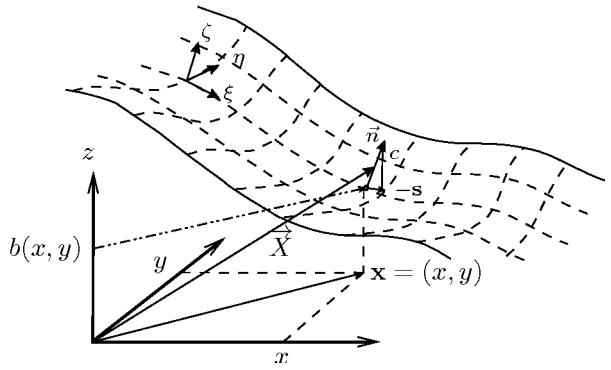

Figure 2. Coordinate systems: the Cartesian coordinates (x, y, z) and the terrain-fitted coordinates (ξ, η, ζ).

[*Jiang and Tadmor*, 1997; *Liu et al.*, 2007]. The time interval is determined by the Courant-Friedrichs-Lewy (CFL) condition. This scheme has been extensively applied in many applications to avalanches and the reader is referred to the relevant papers: *Tai et al.* [2002], *Wang et al.* [2004], *Pudasaini et al.* [2005a, 2005b], and the review by *Pudasaini and Hutter* [2007].

3. Friction Coefficient and Its Calibration

[18] In the present model, Coulomb friction is used to model the drag force during the landslide. The force is assumed to be linearly proportional to the flow pressure on the basal surface with a constant ratio, μ, the friction coefficient. The coefficient is customarily associated with the friction angle ϕ by $\mu = \tan\phi$. Therefore, an accurate estimation of the frictional property of the basal surface is crucial for conducting the numerical simulation of the landslide. The friction coefficient is determined using two methods: The first is the rotary-shearing tests of rocks, and the second is the numerical parameter back-analysis comparing the data from the simulation with that of the field survey.

3.1. Rotary-Shearing Test

[19] Experimental studies on high-speed friction of earthquake faults started with the development of the rotary-shear friction apparatus in the 1990s [e.g., *Hirose and Shimamoto*, 2005; *Di Toro et al.*, 2006; *Han et al.*, 2007]. Recently, researchers have performed rotary-shear tests under an *in-situ* stress condition to measure the basal friction coefficient of landslide materials [*Miyamoto et al.*, 2009; *Yano et al.*, 2009]. Because of technological limits, the maximum achievable shearing speed is about 1.3 m/s. Although this is still far below the maximum speed of avalanche flows, the measured friction coefficient is by-far the most direct evidence of the low friction coefficient once the rupture and the landslide motion take place. The description of the *high-speed* friction apparatus and the experimental procedures can be found in the works by *Togo et al.* [2009], *Mizoguchi et al.* [2007], and *Kitajima et al.* [2010].

[20] The mass of the Hsiaolin landslide consisted mainly of Pliocene shale and colluvium; see the auxiliary material and *Dong et al.* [2011]. Therefore, both materials were collected for the test. The thin, black colluvium, disturbed by the landslide just above the bed rocks, was sampled using a shovel near the source scar area (solid red circles in Figure 1b). The shale, on the other hand, was prepared by crushing and grinding from 25 mm intact cores of the shale rock, sampled using a portable drilling machine on the slip surface (solid red squares in Figure 1b). The initial particle size of both types of the samples was finer than 1 mm. It is speculated that these sample materials were similar to those on the basal surface. The natural water contents of total 31 colluvium samples were distributed between 9% and 25%, Figure 3a. Accordingly, the following samples were selected in the test: one colluvium sample with a natural water content of 23% by weight, one colluvium sample with 10%(wt) added pure water, and one shale sample with 20%(wt) added pure water. These samples were assumed to provide good coverage of the water content of the landslide material during the landslide.

[21] In the tests, the sample powders were sandwiched in between a pair of solid-cylindrical rock specimens (Belfast dolerite) (Figure 3b). The diameter of the two holding rock cylinders was 25 mm; the filling gap for the sample powder was about 1 mm and the total sample weight in each test was about 1 gram. The contact surfaces of the cylinders were deliberately roughened to ensure that the shearing deformation would take place within the sample, and a Teflon sleeve was mounted to hold the sample powder and its water content while shearing was applied. To mimic the *in-situ* normal stress on the basal surface with a 40 m thick avalanche layer, the samples were sustained under a normal stress of around 1 MPa during tests. The shearing speed was adjustable up to 1.3 m/s. The shearing speed was defined as the quotient between the total shear work and the equivalent slip rate [*Hirose and Shimamoto*, 2005]. The friction coefficients were then inferred by calculating the ratios between the reacting torques and the applied normal stress [*Kitajima et al.*, 2010].

[22] There are two additional concerns about the rotary tests. The Teflon sleeve could not fully prevent water or heated steam escaping from the sample compartment because of the shear-induced and thermal pressurization. There hence existed complex pore pressure effects during tests. However, these effects were implicitly lumped into the calculation of the friction coefficient because the total stress approach was applied. Because fluids probably could escape more easily from our small specimen assembly than in the natural landslide, the measured friction was probably an upper bound for friction that occurred in the real scenario. The other concern is that Teflon may be decomposed due to Teflon-rock friction. Fluorine from decomposed Teflon may enter into the gouge sample because fluorine-containing crystals were recognized occasionally near the Teflon contact. It is doubted however that Teflon pieces intrude deep into the gouge sample under pressure. Even if they did, the Teflon pieces did not affect the observed behavior because the tests with gouge containing Teflon pieces up to a few tens of percents (by weight) did not show significant changes in the frictional behavior [*Kitajima et al.*, 2010, section 4.4].

[23] Figure 3c shows the experimental results of the high-speed frictional tests. The vertical axis is the friction coefficient, and the horizontal axis is the shearing distance, i.e. the product of the shearing speed and the elapsed time from the instance at which the constant shearing-speed was applied. These samples had similar properties: The maximum friction

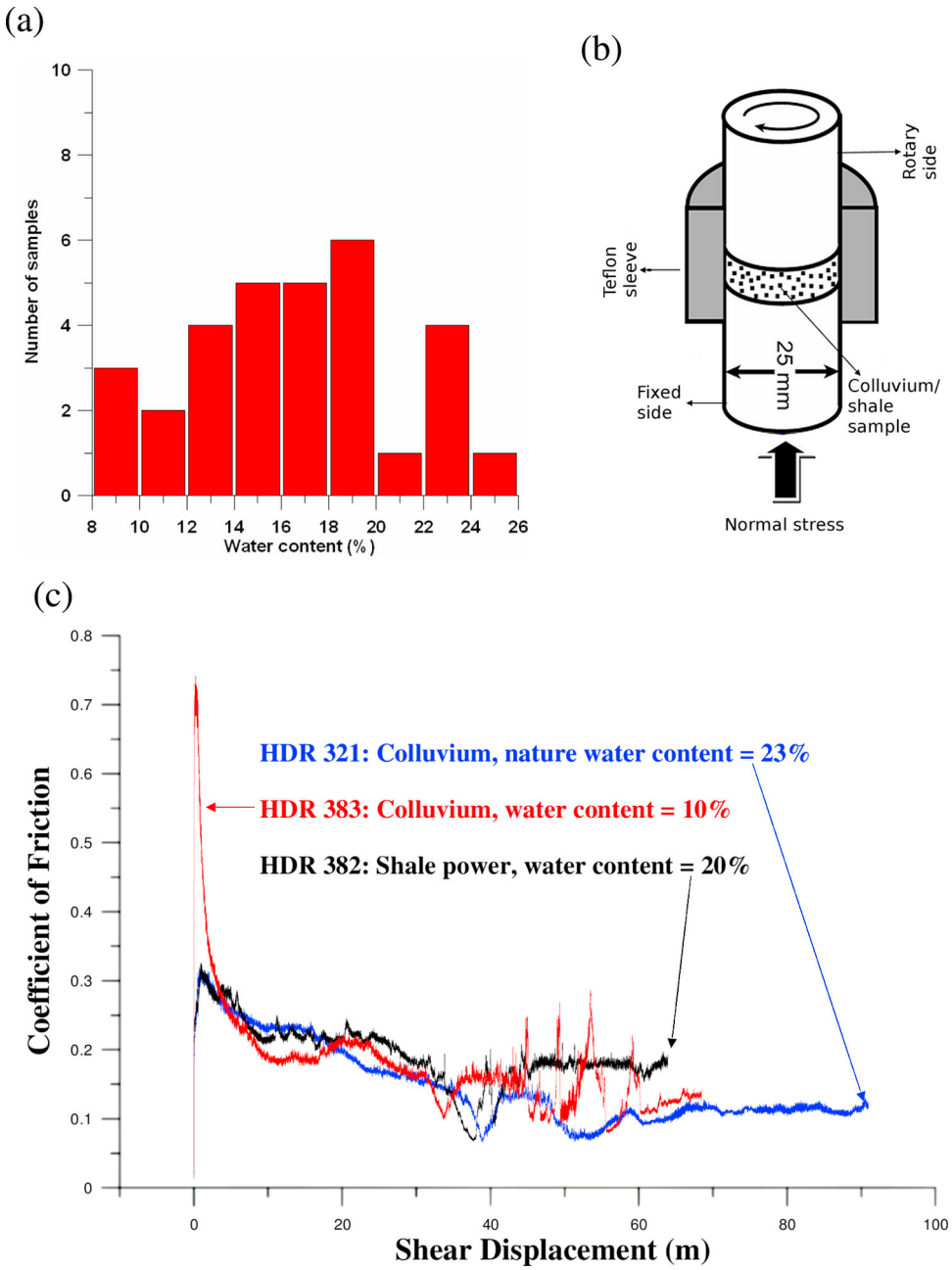

Figure 3. Measurement of friction coefficients. (a) Water content distribution of the samples. (b) The rotary shear cell. The samples were sandwiched between two dolerites as host rocks and tested under room temperature and humidity. The normal stress was 1 MPa and the shearing speed, 1.3 m/s. (c) The friction coefficients versus the accumulative shearing displacement. The shearing distance is defined as the product of the shearing speed and the elapsed time when the shearing is applied [*Hirose and Shimamoto*, 2005]. The colluvium and shale samples were collected from the landslide field. Sample HDR 382 (shale powders) was prepared with crushed, dried shale core with added pure water at 10% by weight. Sample HDR 383 was colluvium with the water content at 10% by weight. Sample HDR 321 was colluvium with (preserved) saturated natural water content (23% wt).

coefficients occurred near the initial moment, and their values rapidly dropped to constants as the shearing progressed. The friction coefficients can be expressed as a function of the shear displacement, the shear velocity and the normal pressure, which is referred to as the velocity-dependent friction law [*Han et al.*, 2010].

[24] For the present samples, the peak friction coefficients were about 0.3 except that of the sharp initial peak of the colluvium of 10% water. The constant steady state friction coefficients were between 0.1 and 0.2, and the colluvium samples had the lower values. See also the auxiliary material for additional tests with the shale samples. The data indicated

that the friction coefficient rapidly reduced to the steady state values within a few meters of slip. Although the friction in the rotary tests was caused by the yielding within the sample material, the inferred friction coefficient represented the capability of providing the resistive force versus the normal pressure by the thin shearing layer between the moving part against the stationary part. On natural terrains, the shearing layers of landslides were formed adjacent to the basal surface with similar material composites to both sides of the test samples. It was, hence, conjectured that the friction coefficient on the basal surface was close to the constant steady state values measured in the experiments and remained on this level for nearly the entire motion of the landslide. Similar close correlation between the measured friction coefficient and the back-analysis simulation was also found previously by comparing the results from separated experimental and theoretical studies on the Tsaoling landslide [*Miyamoto et al.*, 2009; *Kuo et al.*, 2009]. The landslide was triggered by the Chi-Chi earthquake in Taiwan, 1999, and had a sliding mass about five times of the present Hsiaolin landslide. The correlated friction coefficient was at a much lower value (about half).

3.2. Empirical Scaling Laws

[25] After the landslide was initiated, the moving block collapsed and transformed into granular flows. No direct measurements have been conducted when real landslides were in motion and no laboratory experiments have been performed with matching conditions of real landslides, see section 3.1. Therefore, the friction coefficients were generally obtained by the statistical regression analysis for real landslides. The friction coefficients were often expressed in terms of landslide volumes, V, traveling distances, L, and descending levels, H [*Scheidegger*, 1973]. The statistical analysis, together with other similar approaches, in the references in the work by *Legros* [2002], led to the well known phenomenological conclusion that the friction coefficient was inversely correlated to the landslide volume. On the other hand, based on the balance of the total energy and frictional dissipation, an alternative expression for the effective friction coefficient, $\mu_e = H/L$, was obtained [*Heim*, 1932; *Staron and Lajeunesse*, 2009].

[26] Because of the complexity of the natural geological contents, the definition of physical variables was subjected to some uncertainties. In this study, the gravity centers of the measured scar and deposit volumes were used to estimate the associated parameters which yielded an end-to-end displacement L = 2000 m and H = 460 m. Based on the precision of the DTMs, a couple of tens of meters error bounds in the estimation were expected (assuming a few folds of the standard deviation of the DTMs, see section 4). With these parameters, the effective friction coefficient was approximately 0.23 ($\approx H/L$), or 0.29 (Scheidegger's regression formula). The standard deviation, as given by *Scheidegger* [1973], was 0.14. Using a similar method, *Tsou et al.* [2011] quoted the apparent friction coefficient to be 0.25. These values, however, may have been somewhat overestimated because the traveling distance L was underestimated. There were two main reasons why L was underestimated: (1) the traveling distance was constrained by the slope on the west bank of Cishan river such that the landslide flow was redirected into the river valley, and (2) the flush-away debris by the follow-up dam breach was neither included in the calculation of the gravity center which led to the underestimation of the traveling distance. With the above consideration in mind, it was conjectured that the friction coefficient value was on the negative side of the quoted values.

[27] These statistical-based analyses were referred as the empirical scaling laws. The reverse dependence of the friction on the landslide volume was the one of the most intriguing characteristics of landslides and it was called the volume-induced lubrication [*Staron and Lajeunesse*, 2009]. *Davies* [1982] pointed out that debris spreading played an important role in the volume-dependent phenomena. The spreading length L_* and the total volume has a regression relation $L_* = 9.98\ V^{0.32}$. With the volume of the present landslide, the spreading length was estimated 2300 m by the formula compared to the measured 1600 m in the real deposit (the widest spreading direction, NWW-SEE). The discrepancy between the two values was still within the margin of errors among the real landslide data although the valleys of Cishan river and Anonymous Creek provided constraints for the spreading. From the above comparison, the Hsiaolin landslide was not a statistical outlier.

[28] *Staron and Lajeunesse* [2009] further argued that the landslide runout can be decomposed into two contributors: sliding and spreading. The indicator for determining the dominant contributor in the runout is the ratio between the vertical projection of the characteristic length of the landslide mass and the descending level. This ratio is explicitly $V^{1/3}/(H \sin\theta)$ for a three-dimensional terrain where θ is the inclination angle of the slope. Taking the average inclination angle, 15°, of the Hsiaolin Slope for θ, the ratio was 2.2 which was greater than one and therefore the runout was dominated by the spreading of debris according to *Staron and Lajeunesse* [2009].

[29] Based on the previous discussion and findings, the initial guess of the apparent friction angle was set to 0.2. This value was also in the acceptable range of the apparent friction coefficients found by discrete element simulations [*Campbell et al.*, 1995; *Legros*, 2002; *Wu and Chen*, 2011]. The coincidence between the chosen value and the constant steady state values found in the rock tests indicated that the transit of the friction coefficient from the low speed landslide initiation to the high speed flow regime was smooth. A question now to be answered is whether the simulation with this friction coefficient value or the nearby values can lead to agreeable simulation results with respect to the real deposit. For this purpose, an iterative scheme for the optimal friction coefficient by minimizing the discrepancy between the simulation and the field measurement is proposed. The procedure is described in section 3.3.

3.3. Numerical Calibration

[30] Instead of a heuristic determination of the rheological parameters based solely on the shape of the deposit outlines, an optimization process is proposed in this section. The process minimizes an object function, which is defined to be the deviation between the simulation and the deposit, over the rheological parameter domain. For the Coulomb friction, the parameter domain consists of only one parameter: the friction coefficient μ. The object function is defined as the average of the square of the difference between the

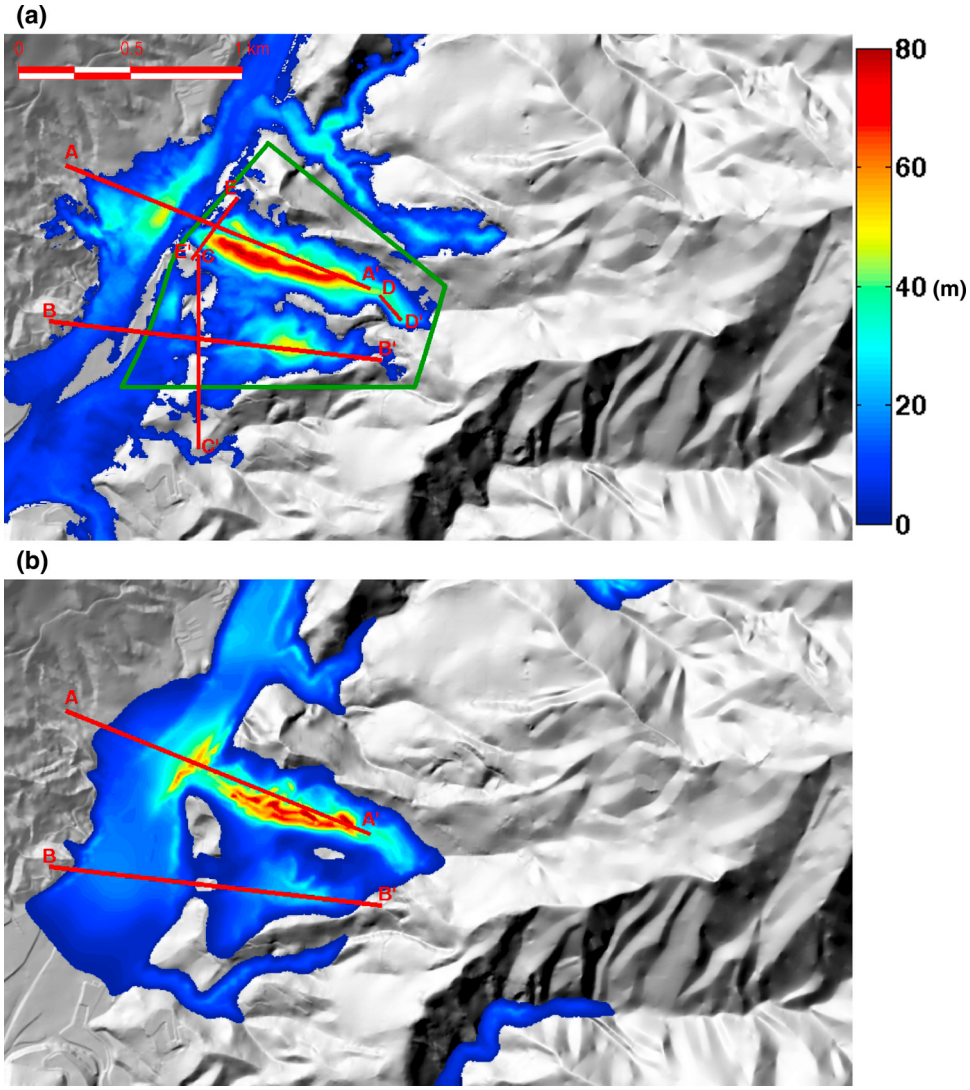

Figure 4. (a) Actual deposit (after the dam breach) and (b) simulated deposit (without dam breach). The deposit depths are coded with the same color axis. The area boxed by the bold dark green polygon is the region for the minimization scheme (7). Five profiles are defined for detailed inspection. Profiles $\overline{AA'}$ and $\overline{BB'}$ are for comparison of the deposits in Anonymous Creek and the Hsiaolin Slope. Profiles $\overline{CC'}$, $\overline{DD'}$, and $\overline{EE'}$ are for volume flux calculations.

simulation and the measurement over the main deposit area. Therefore, the optimization scheme reads

$$h_{std}^2(\mu) = \min_{\mu} \frac{1}{A} \int_A (h(\mathbf{x};\mu) - h_{meas}(\mathbf{x}))^2 \, dA \qquad (7)$$

where $h_{std}(\mu)$ is the standard deviation between the two compared deposit depths, $h_{meas}(\mathbf{x})$ and $h(\mathbf{x};\mu)$. The $h_{meas}(\mathbf{x})$ is the measured deposition depth and the $h(\mathbf{x};\mu)$ is the simulated depth with the friction coefficient μ. The A is the area of the main deposit zone. The simulation time is set sufficiently long, here 180 s, to ensure that the flow speed in the main deposit area is less than the average 2 m/s, 4% of the maximum flow speed, at the end of the simulation. The main deposit zone, which is the area of interest, was made slightly larger than the union area between the simulated and measured deposits. For simplicity and robustness in the minimization procedures, the simplex method is used [*Nelder and Mead*, 1965]. It is also possible to automate the regression processes by more sophisticated optimization schemes for better optimization efficiency. To conclude, by using the present optimization process, the subjective visual inspection of the simulation results, which was commonly seen in practice, is eliminated.

[31] It is often argued that the water content and debris collision in avalanche materials introduce a flow drag to the landslide motion. This fluid drag force is referred to as turbulent drag. *Voellmy* [1955] assumes that it is a term in addition to the Coulomb friction force and is proportional to the square of the flow speed. Following the same derivation as in section 2 and assuming that the turbulent drag is of the same order of magnitude as the frictional force, the same model equations as (3) are obtained, but with the momentum source replaced by [see also *Hungr and*

Table 1. Minimization Iterations[a]

Iteration Number	Friction Angle ϕ (deg)	Depth Deviation (m)
1	11.40	7.651
2	11.50	7.612
3	11.45	7.611
4	11.47	7.610
5	11.47	7.610

[a]The friction coefficient μ is related to the friction angle ϕ by $\mu = \tan\phi$. The convergence condition of the minimization is set to 0.01.

McDougall, 2009; *Kelfoun and Druitt*, 2005; *Schneider et al.*, 2010]

$$\varsigma_\xi = -J_b N_b \mathbf{s} - \frac{\mathbf{u}}{||\vec{u}||} J_b \left[\mu N_b \mathbf{s} + \frac{1}{\alpha} ||\vec{u}||^2 \right]. \quad (8)$$

The second term in the square brackets of (8) represents the turbulent drag, with an additional dimensionless constant rheological parameter α. To complement the present simulation, the turbulent coefficient α is also calibrated for comparison.

4. Simulation

[32] Aerial photograph interpretation and mapping are routinely performed by the Agricultural and Forestry Aerial Survey Institute of Taiwan. In 2009, the institute released the digital terrain model (DTM) of the Hsiaolin area (photographed on 7 January). It was acquired by aerial photography technology. After the landslide, an updated DTM was derived using aerial photos taken on 13 August 2009 by the same institute with the same method and analysis settings. The flight routes and the aerial photography cameras were arranged to ensure that the resolutions of ground images were higher than 30 cm/pixel. The DTMs acquired from the photograph interpretation have a horizontal resolution of 5 × 5 m with a total image unit weight RMSE (root mean square error) of less than 1 m. The precision of the pre/post-event DTMs was evaluated by inspecting the elevation deviation for regions without visible slope failures. Five such regions (see auxiliary material) were identified. The average elevation difference was about −0.4 m and the elevation standard deviation was 2.9 m. Subtracting the two DTMs, the scar and the deposit areas were identified (cf. Figure 1). The deposit has been re-sketched in Figure 4a, in which the small scale and thin deposits outside the main deposit area have been filtered for clarity.

[33] The computational domain was 3,710 × 2,220 m^2. The topography was coarsened by selecting every alternative grid in the DTMs to a 10 × 10 m^2 mesh and processed with a spatial Gaussian filter to eliminate high wavenumber irregularities for better numerical performance and convergence. The standard deviation caused by these artificial adjustments are smaller than 0.9 m, which is in the range of the precision error of the DTMs. The initial volume was set directly from the DTMs without a presumed volume dilation. In the simulation, there were two scar areas: the main scar and the 590 Height scar. The sliding volume of the former was (24 ± 2) × 10^6 m^3 and that of the latter was (1.5 ± 0.2) × 10^6 m^3. The sliding mass was released at $t = 0$. Along with the main sliding mass, the secondary landslide mass, the 590 Height scar, was released simultaneously for simplicity; i.e., the impact of the main slid mass onto the 590 Height was neglected. Different release conditions were tested but no significant changes to the main flow were found because the volume of the 590 Height was only about 6% of the total.

[34] When applying continuum models to landslides, such as the present model, one assumption is automatically made. This assumption is that the fracture mechanisms of the sliding mass are neglected. These fracture mechanisms include the rock buckling failure, crack propagation etc. The fracture procedures of the landslide mass are therefore assumed to be completed shortly after initiation such that the fluid model can work. This may be an acceptable assumption because the propagation of internal cracks are of the order of sound speed in rocks which is much faster than the flow speed. This assumption was also made by *Kuo et al.* [2009]. For readers who are interested in the fracture mechanisms, alternative simulation tools such as discrete

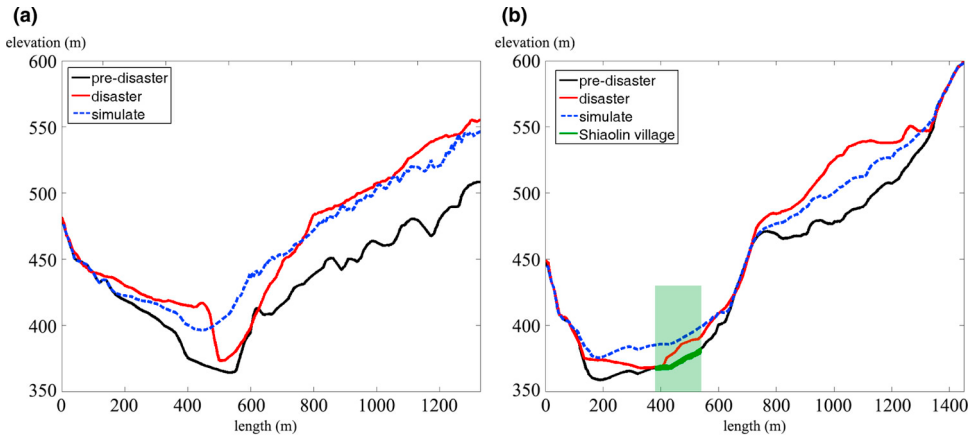

Figure 5. Comparison of the actual and the simulated deposits on (a) the $\overline{AA'}$ profile, Anonymous Creek, and (b) the $\overline{BB'}$ profile, the Hsiaolin Slope. Points A and B are the origins of the x–axes in Figures 5a and 5b. The black lines are the original basal topography, the red lines are the post-event topography, and the blue dashed lines are the simulated deposits. The green shaded regions indicate the location of the village.

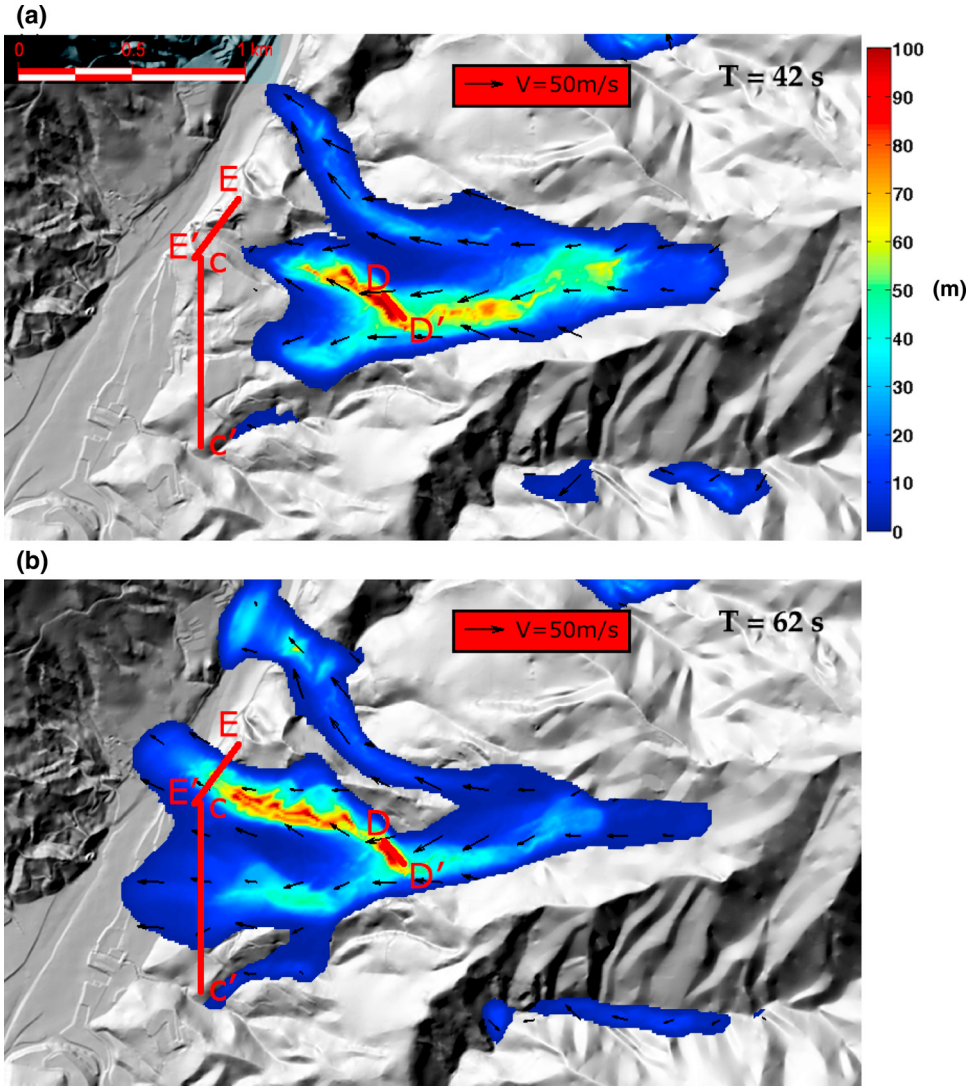

Figure 6. Landslide snapshots at (a) t = 42 s and (b) t = 62 s. The profiles were defined for volume flux calculations. Profile $\overline{CC'}$ was defined to capture the volume flux flowing into the village, profile $\overline{DD'}$ was for resolving the 590 Height impingement, and profile $\overline{EE'}$ was for estimating the arrival of the landslide at the Cishan River bank. The arrows represent the flow velocity, and the maximum speed was about 50 m/s along Anonymous Creek.

element methods could be used [*Campbell et al.*, 1995; *Chang et al.*, 2005].

[35] Before using the minimization scheme, described in section 3.3, to determine the accurate friction coefficient, two prerequisites are to be used: the deposit area for the parameter calibration and the initial estimation of the friction coefficient. Because there was a dam breach after the landslide in the Hsiaolin catastrophe, most of the deposit in the Cishan River channel was flushed away, and a new river channel was quickly formed by the streamflow before the aerial measurements were performed. To eliminate the errors caused by the dam breach, the Cishan River valley was excluded from the minimization process. The remaining deposit area was the Anonymous Creek Valley and the Hsiaolin Slope, the slope towards the Hsiaolin township. The resultant area for the calibration was defined as the region surrounded by the bold red outlines in Figure 4a.

[36] The initial estimation of the friction coefficient was obtained by referring to the rotary-shearing tests and the empirical scaling laws (sections 3.1 and 3.2). The initial guess of the apparent friction coefficient was set to 0.2 (friction angle 11.31°). For convenience, the minimization scheme was started at friction angle 11°. For each iteration, the simulation time was 180 s, and the outflow condition was applied on the domain boundaries. The progress of the minimization is tabulated in Table 1. The optimized friction coefficient was calibrated to $\mu = \tan(11.47°) = 0.203$, which had only a minute difference from the empirical law. The minimization scheme was also performed for the Voellmy friction law, (8), and the parameters converged to $(\mu, \alpha^{-1}) = (0.194, 8.75 \times 10^{-4})$ with a standard depth deviation of 7.75 m. These parameters formed an adjacent local minimum of the object function that was slightly worse than the case with Coulomb friction alone. Nevertheless, the flow details

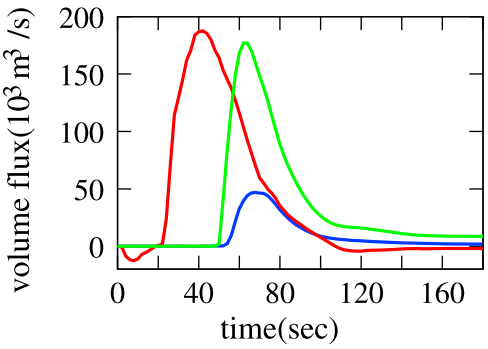

Figure 7. Transient volume fluxes across the profiles defined in Figure 6. The red line is for $\overline{DD'}$, the green line is for $\overline{EE'}$, and the blue line is for $\overline{CC'}$.

were almost identical to the flow with the Coulomb friction because the contribution of the turbulent drag to the landslide flow was found to be much smaller than that of the Coulomb friction. In addition, assuming a constant volume dilation of 20%, the minimization scheme were repeated for both rheological laws (Coulomb and Voellmy). It was found that the best-fit rheological parameters were $\mu = 0.200$ for the Coulomb friction and $(\mu, \alpha^{-1}) = (0.193, 4.21 \times 10^{-4})$ for the Voellmy law. These parameters with the dilated sliding volume deviated only slightly from those without the volume dilation, indicating that the effect of the volume dilation factor on the rheological parameters was negligible.

[37] Because the results of both the Coulomb and Voellmy friction laws were quantitatively similar, the case of the Coulomb friction was focused in the following discussion. The simulated deposit is depicted in Figure 4b. Except for the minor valleys north and south, good agreeable results were achieved in the calibration region. The deposit in the Cishan river channel was, however, more confined in the downstream section (the lower-left corner) compared to what was observed in the field. The total simulated deposit in the calibration region was about 11.5 million m^3, less than the 13 ± 3 million m^3 from the measurement, and the depth deviation was 7.6 m. The simulated deposit in the river channel was roughly 14.1 million m^3 (before being washed away by the dam breach). The deposit volume was probably slightly underestimated because no volume dilation was presumed in the simulation. For granular flows or landslides, the volume dilation ratio is customarily between 10% and 20%, and at this ratio, the discrepancy between the simulated and measured deposit volumes can be largely explained.

[38] To further inspect the deposits in detail, two profiles were defined, $\overline{AA'}$ and $\overline{BB'}$. They cut through the deposit along the centerlines of the Anonymous Creek Valley and the Hsiaolin Slope and were extended across the Cishan River to the opposite river bank. The deposits on the profiles are drawn in Figure 5. An excellent agreement between the simulation and the measurements in the Anonymous Creek Valley was obtained. A maximum discrepancy of about 50% in depth, however, was found in the Hsiaolin slope. This was because the west end of the $\overline{BB'}$ profile was near the 590 Height where the impact between the landslide flow and the height was not correctly simulated (simplified). This implies that the momentum reduction due to the impact as the flow entering the Hsiaolin Slope was somewhat underestimated in the simulation and thus deferred its deposition

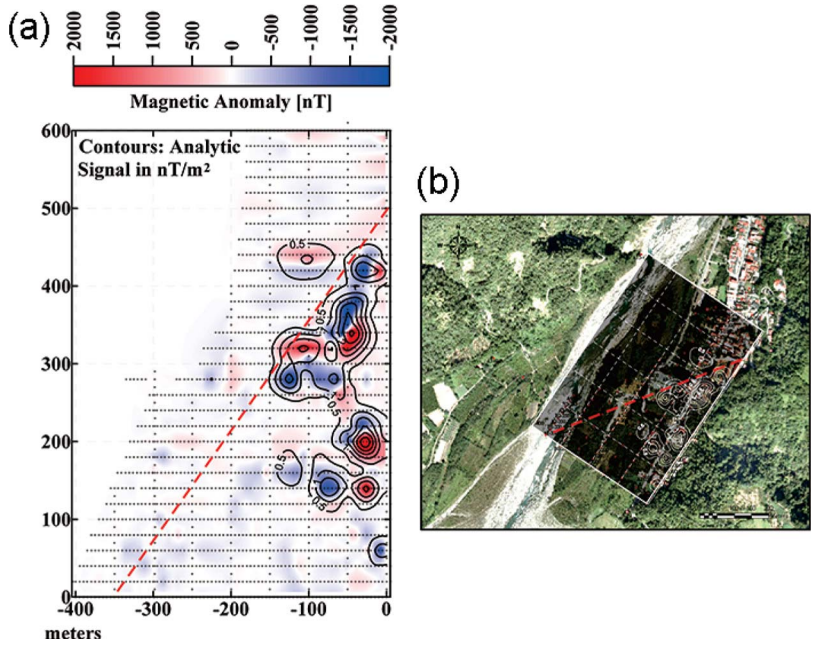

Figure 8. (a) Magnetic anomaly (colors) and amplitude of the magnetic zeroth-order analytic signal (contours) over the main area of Hsiaolin Village. Crosses denote the survey locations. (b) Aerial photograph taken before Typhoon Morakot, superimposed with the magnetic analytic signal (white contours). The thick red dashed line in each panel depicts the sharp destruction boundary of the debris suggested by the results of the magnetic survey.

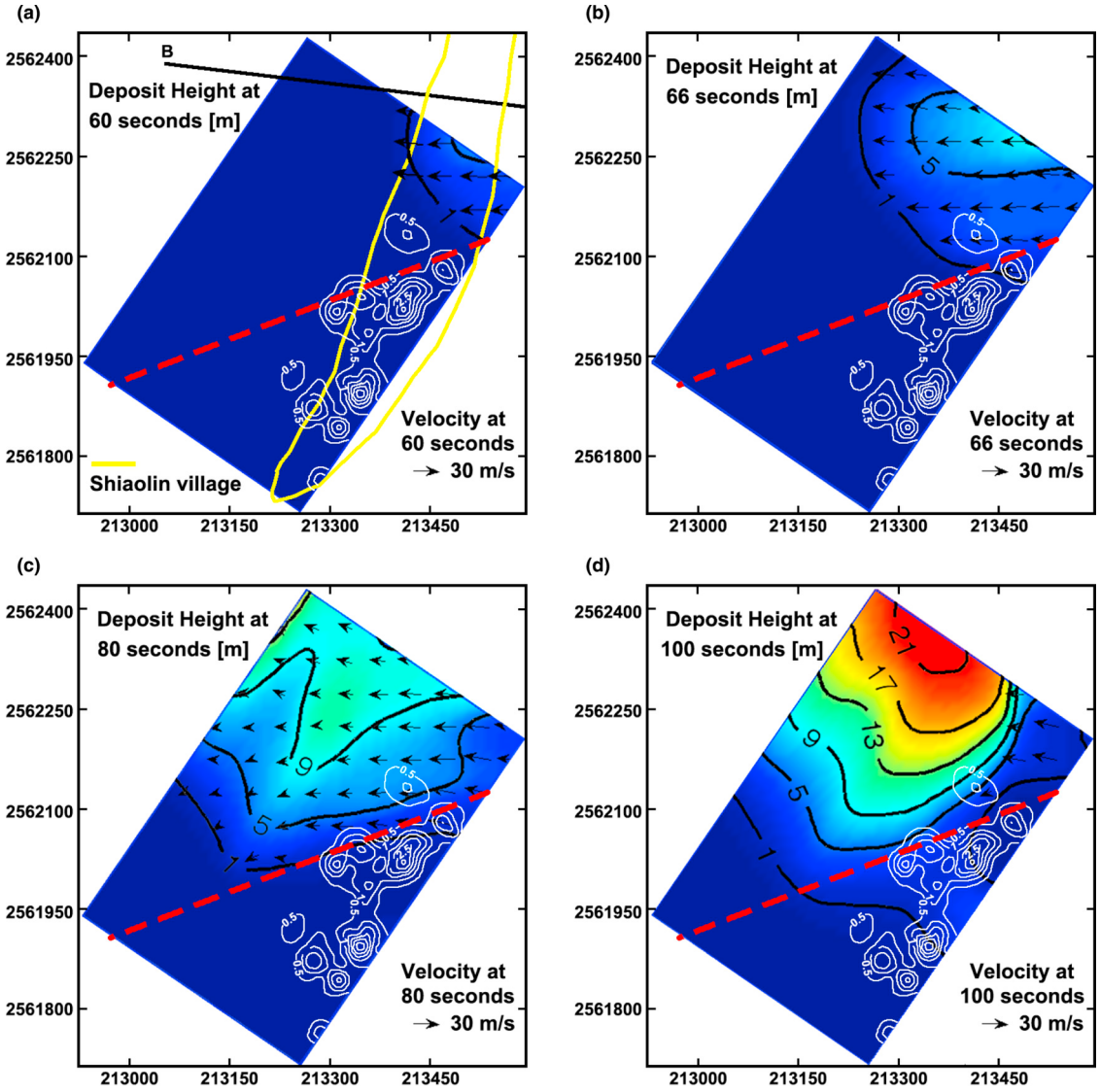

Figure 9. The flow snapshots in the region of the near-surface magnetic surveys. The time-steps were chosen in the peak flux period, see the $\overline{CC'}$ flux in Figure 7. The village area is enclosed by the yellow line. The thick bold black line is the east part of Profile $\overline{BB'}$. The profile cuts almost perpendicularly to the landslide flow front. The thick dashed line indicates the boundary of the landslide flow defined by the magnetic surveys. The magnetic anomalies are superimposed for comparison. The color axis, from dark blue to red, represents flow thickness from 0 to 25 m. The arrows represent the flow velocity.

on the slope. In addition, the solid properties, such as the internal friction angle, angle of repose, and earth pressure properties, of the landslide materials, which are largely omitted in the present model, may also have contributed in part to the discrepancy. From a comparison of the left halves of the profiles in the Cishan River channel, the effects of the second stage dam breach were identified and the excavation mechanism reshaped the river. The simulated deposit volume in the river has been applied in a hydrological study of the dam breach stage of the event [*Li et al.*, 2010].

[39] The shape of the simulated deposit has common feature that is commonly seen in simulations using the continuum model. This feature is that the deposit surface is usually smoother than the real deposit of landslides [see *Kuo et al.*, 2009]. The reason is that the resting surface slope in the model, with the present simplifications, is constrained only by the basal friction. This theoretical property can be seen by substituting $\mathbf{u} = 0$ into the model equations, which leads to the equation for the surface slope in terms of the friction and the gravity force. Incorporating the internal friction angle, the solid constitutives, such as the Mohr-Coulomb material law [*Denlinger and Iverson*, 2004; *Kelfoun and Druitt*, 2005; *Crosta et al.*, 2009], or the erosion/deposition mechanism [*Tai and Kuo*, 2008; *Tai and Lin*, 2008; Tai et al., submitted manuscript, 2011], may further improve the accuracy of the simulation. However, applying these additional constitutive relations and erosion/deposition mechanisms would involve solving the internal stress states of the flow in detail which challenges the numerical convergence, stability, and the justification of the

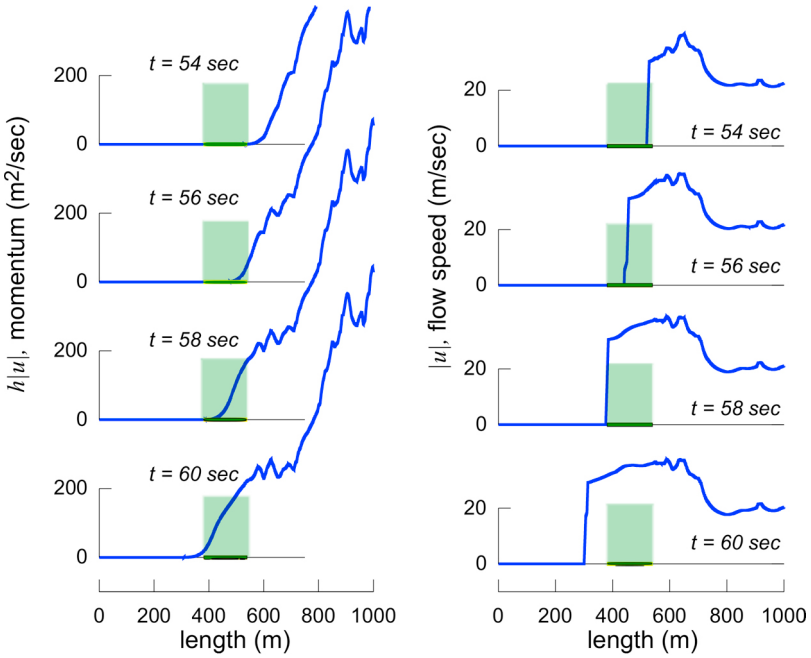

Figure 10. (left) Momentum and (right) velocity on profile $\overline{BB'}$. The green shaded regions indicate the location of the village. Point B is the origin of the x–axis. The figures show the progress of the landslide front. The flow speed was about 35 to 40 m/s when it swept over the village which may be somewhat overestimated because interactions with the village buildings were neglected in the model.

extra rheological parameters. It is therefore beyond the scope of the present paper. In the literature, both *Denlinger and Iverson* [2001] and *Kelfoun and Druitt* [2005] performed simulations with considerations of earth pressure coefficients which brought certain solid properties of the landslide materials into the landslide flow. Along the line of research, further investigations with these solid properties for this Hsiolin landslide were initiated.

[40] Having confirmed the deposits, the landslide motion was to be examined. Two snapshots at $t = 42$ s and $t = 62$ s are shown in Figures 6a and 6b. These time steps corresponded to the peak landslide flow at the 590 Height and the west bank of the Cishan River. Upon hitting the 590 Height, the flow split into two runout paths (Figure 6a). The mainstream was diverted to flow along the Anonymous Creek Valley, and the second flow moved through the southern part of the 590 Height into the Hsiaolin Slope and the Hsiaolin village. The maximum speed was as fast as 50 m/s along the main runout path. This maximum speed agreed well with the seismological inversion analysis of seismic signals captured by the seismic stations [*Chen*, 2010; *Lin et al.*, 2010; *Stark et al.*, 2010]. This agreement echoed the growing interest and research achievements on the study seismic responses of landslides [see, e.g., *Ekström et al.*, 2003; *Schneider et al.*, 2010].

[41] Three key features of the Hsiaolin landslide remain to be further addressed: (1) the first impression on the impact of the flow upon the 590 Height; (2) the approach of the mass flow to the Cishan River valley; and (3) the flow towards the village. For these purposes, three profiles, $\overline{DD'}$, $\overline{EE'}$, and $\overline{CC'}$ were defined and the landslide volume fluxes crossing these profiles were calculated by integrating over the length of the profiles. They are plotted in Figure 7.

[42] A few marking time-stamps were first identified. The landslide reached the 590 Height at 50 s. There was a small negative preceding flux which was the result from the simplified instantaneous release of the materials of the 590 Height. Then the flux quickly peaked at 42 s. Diverted by the 590 Height, the landslide flow split into two parts as previously discussed. The split fluxes arrived at the Cishan River bank, $\overline{EE'}$, and flowed toward the village, $\overline{CC'}$, at almost the same time, about 50 s, and both reached the maxima at about 62 and 64 s. The landslide motion came to rest within about 110 s, and in the model the fluxes became less than 10% of the maxima.

[43] The profile $\overline{CC'}$ was defined adjacent to the Hsiaolin village, which allowed capture of the volume flux flowing through the village. Integrating the volume flux with respect to time, it was found that the total debris volume through the village was about 1.58×10^6 m^3, only roughly 7% of the sliding volume. This volume, however, was the most devastating branch of the landslide stream, and it will be examined in detail in section 5.

5. Near-Surface Magnetic Survey and Flow in the Village

[44] The near-surface magnetic survey was performed by using high sensitivity magnetic sensors (Geometrics model G-856, with a sensitivity of 0.1 nT) to measure the total magnetic field strength on the ground surface. Because the magnetic field reacted strongly to magnetizable materials such as iron and steel, anomalies caused by the buried artifact structures/objects, e.g., reinforced concrete structures and cars, can be detected by the magneto-meters and analyzed. With this technology, a set of high-resolution (20 × 5 m)

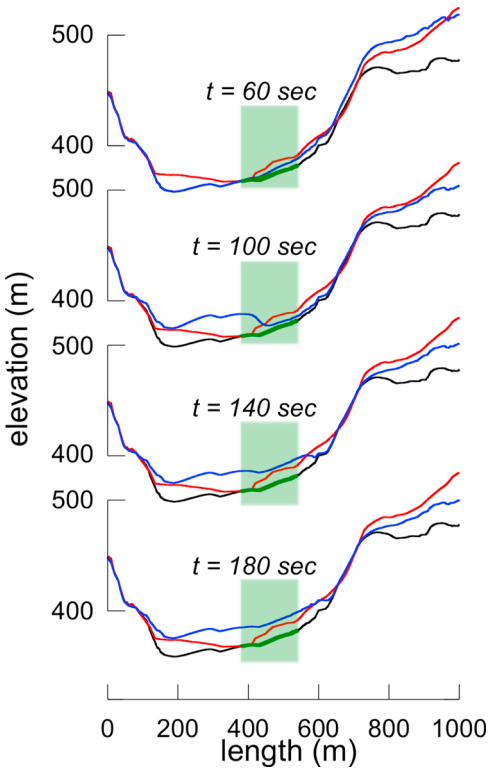

Figure 11. Flow depth on profile $\overline{BB'}$. Point B is the origin of the x–axis. The black line is the original basal topography, the red line is the post-event topography, and the blue line is the simulated deposit. The green shaded regions indicate the location of the village. The figure shows that the thick deposit was formed by the debris surge being reflected by the slope on the opposite side of the Cishan River. The thickness over the village was about 17 m. The regress, or discrepancy between the simulation and the field survey, in the river channel was caused by the dam breach after the landslide.

near-surface magnetic data covering the main township of Hsiaolin Village was obtained. The survey was performed in October 2009, the month after the landslide occurred. The instruments and technical details can be found in the work by *Doo et al.* [2011].

[45] The magnetic anomaly map (colors in Figure 8a) presents the anomalous patterns of the magnetic dipole fields, and it can be used to derive the amplitude distribution (contours in Figure 8a) of the zeroth-order analytic signals of the magnetic sources [*Hsu et al.*, 1998; *Hsu*, 2002; *Doo et al.*, 2009]. Superimposing the distributions of the magnetic sources onto the aerial photograph taken before Typhoon Morakot, it was clearly identified that all of the magnetic sources corresponded closely with the buildings located in the southern part of the township, Figure 8b. The sharp boundary of the destruction front of the landslide, the thick dashed lines in Figure 8b, could be defined by a comparison between the magnetic anomalies and the aerial photograph. The results suggested that the buildings located to the north of the boundary were removed from their original locations by the impact of the landslide.

[46] The simulation showed that there was a very destructive front. In Figure 9, snapshots of the landslide flow in the village during the peak flux period were presented. The first three snapshots indicated the propagation of the landslide front and the flow velocity field. The flow entered the village from the north-west side of the village boundary. More specifically, it was near the exit of the Hsiaolin Slope, which was around the midpoint of the $\overline{CC'}$ profile. The flow direction was toward the west. The measured boundary of the magnetic anomalies, the bold red dashed line, were found to be well coincident with the flow boundary, defined by the contour line of 1 m deep. Further south at the boundary, the flow was thinner than 1 m. The simulation hence provided strong evidence that the buildings and the artifact objects in the north of the village were dislocated into the Cishan river by the landslide while in the south, the flow did not have enough momentum to shear off the buildings. After the passing of the flow front, the debris then buried the north side of the village and flowed into the river channel; see the snapshot at t = 100 s.

[47] The kinematic properties of the landslide were examined along the $\overline{BB'}$ profile. The momentum and the velocity are sketched in Figure 10. The time when the flow front swept through the village was specifically analyzed and it was between 54 and 60 s in the simulation. During these moments, the flow speed reached 35 to 50 m/s and the momentum (per unit density) was about 250 m^2/s. The flow height at the impact was 6 to 7 m. A much thicker debris then flooded the village at a much later time, 100 s, in the form of a reflected surge wave (Figure 11). The surge was reflected by the slope on the opposite side of the Cishan River. The final debris deposit was roughly 17 m deep. A similar behavior was also found in the Tsaoling landslide when its debris mass interacted with the foothill river valley [*Kuo et al.*, 2009].

[48] The agreements between simulation and the magnetic surveys on the flow that entered the Hsiaolin village are a critical justification of the simulation model. The achieved good agreements may have been attributed to that the landslide was a spreading dominant flow. In addition to the same conclusion from the empirical scaling laws, it could be also confirmed by the field observations that the deposit was composed of grains from fine particles (sub-millimeters in size) to shale blocks with sizes up to a few meters [*Dong et al.*, 2011]. Comparing to the characteristic lengths of the landslide, say $V^{1/3}$ approximately 290 m, or the flow thickness, approximately 40 m, the grain sizes were small. Hence, the collective behavior of the landslide mass showed the characteristics of fluid flows and can be modeled by the continuum model accurately.

6. Conclusion

[49] The rainfall brought by Morakot typhoon triggered the Hsiaolin landslide and devastated the township of Hsiaolin Village. The event was composed of two sub-events: the landslide and the dam breach. With the present hydrodynamic model, the landslide was accurately reconstructed.

[50] The hydraulic model was derived with considerations of general topography. The model equations used are similar to the shallow water equations and are written in a

conservative form with the flow depth and the Cartesian velocity as the unknowns. The rotary-shearing tests of the rock properties and the empirical friction scaling laws both indicated that the friction coefficient was about 0.2. This estimated friction coefficient value was confirmed by the numerical calibration based on the minimization of the difference between the simulation and the measurements. The Voellmy friction law was also tested which yielded a virtually identical landslide flow. The volume dilation, assumed up to 20%, also showed an insignificant effect on the rheological parameters.

[51] The main deposit of the landslide was in the Anonymous Creek and on the Hsiaolin Slope. Its maximum speed reached about 50 m/s, and the overall landslide duration was about 110 s. The simulation also showed that there was one branch stream of the landslide debris created as the result of the landslide impact on the 590 Height, and it was this stream that overflowed the Hsiaolin Slope into the village. Even though it was only a minute portion of the landslide mass, this branch stream was the most devastating flow, sweeping over the northern part of the village at a speed of 40 m/s. Its destruction of the village was confirmed by corroboration of the near-surface magnetic measurements and the flow details of the simulation. This good corroboration is also the key validation of the landslide model for its applicability in landslide assessments. The simulation deposit in the river channel has been further integrated with hydrology calculations to resolve the second stage dam breach sub-event [*Li et al.*, 2010].

[52] The Hsiaolin landslide was a large-scale geological failure, and the topography of the runout path significantly influenced the flow direction. This large-scale geological failure urges us to initiate detailed surveys to identify potential hazardous sites further beyond shallow slope failures. The surveys must include predictions of the landslide pathways and deposits with topographies properly taken into consideration. The present benchmarks demonstrate that the hydrodynamic model can be a valuable analytical tool for this purpose.

[53] **Acknowledgments.** This work was supported in part by the National Science Council under the grants NSC 98-2745-M-008-013 and NSC-99-2116-M-001-015. The critical reviews by T. Davies, K. Hutter, and two anonymous reviewers are deeply appreciated. All authors contributed equally in this paper: C.C.C., J.J.D., and C.T.L. conducted field and magnetic surveys; J.J.D., R.H.H., and T.S. conducted shearing tests; and Y.C.T., K.J.C., A.Y.S., C.Y.K., and C.C.C. performed DEM construction, simulation, and analysis.

References

Bouchut, F., and M. Westdickenberg (2004), Gravity driven shallow water models for arbitrary topography, *Commun. Math. Sci.*, *2*(3), 359–389.

Campbell, C. S., P. W. Cleary, and M. Hopkins (1995), Large-scale landslide simulations: Global deformation, velocities and basal friction, *J. Geophys. Res.*, *100*, 8267–8273.

Chang, K. J., A. Taboada, M. L. Lin, and R. F. Chen (2005), Analysis of landslide by earthquake shaking using a block-on-slope thermomechanical model: Example of Jiufengershan landslide, central Taiwan, *Eng. Geol.*, *80*, 151–163.

Chen, C. (2010), Tragic moment of Shiaolin debris avalanche, Taiwan, reconstructed by near surface geophysical/geological and simulation evidence, *Eos Trans. AGU*, *91*(26), West Pac. Geophys. Meet. Suppl., Abstract T42A-02.

Chen, H., and C. F. Lee (2000), Numerical simulation of debris flows, *Can. Geotech. J.*, *37*, 146–160.

Crosta, G. B., S. Imposimato, and D. Roddeman (2009), Numerical modeling of 2-D granular step collapse on erodible and nonerodible surface, *J. Geophys. Res.*, *114*, F03020, doi:10.1029/2008JF001186.

Davies, T. R. H. (1982), Spreading of rack avalanche debris by mechanical fluidization, *Rock Mech.*, *15*, 9–24.

Denlinger, R. P., and R. M. Iverson (2001), Flow of variably fluidized granular masses across three-dimensional terrain: 2. Numerical predictions and experimental tests, *J. Geophys. Res.*, *106*, 553–566.

Denlinger, R. P., and R. M. Iverson (2004), Granular avalanches across irregular three-dimensional terrain: 1. Theory and computation, *J. Geophys. Res.*, *109*, F01014, doi:10.1029/2003JF000085.

De Toni, S., and P. Scotton (2005), Two-dimensional mathematical and numerical model for the dynamics of granular avalanches, *Cold Reg. Sci. Technol.*, *43*, 36–48.

Di Toro, G., T. Hirose, S. Nielsen, G. Pennacchioni, and T. Shimamoto (2006), Natural and experimental evidence of melt lubrication of faults during earthquakes, *Science*, *311*, 647–649.

Dong, J. J., Y. S. Li, C. Y. Kuo, R. T. Sung, M. H. Li, C. T. Lee, C. C. Chen, and W. R. Lee (2011), The formation and breach of a short-lived landslide dam at Hsiaolin Village, Taiwan—Part I: Post-event reconstruction of dam geometry, *Eng. Geol.*, doi:10.1016/j.enggeo.2011.04.001, in press.

Doo, W. B., S. K. Hsu, C. H. Tsai, and Y. S. Huang (2009), Using analytic signal to determine magnetization/density ratios of geological structures, *Geophys. J. Int.*, *179*, 112–124.

Doo, W. B., S. K. Hsu, C. C. Chen, H. H. Hsieh, H. Y. Yen, Y. G. Chen, and W. Y. Chang (2011), Magnetic signature of Siaolin Village, southern Taiwan, after burial by a catastrophic landslide due to Typhoon Morakot, *Nat. Hazards Earth Syst. Sci.*, *11*, 759–764.

Ekström, G., M. Nettles, and G. A. Abers (2003), Glacial earthquakes, *Science*, *302*, 622–624.

Gray, J. M. N. T., M. Wieland, and K. Hutter (1999), Gravity-driven free surface flow of granular avalanches over complex basal topography., *Proc. R. Soc. London, Ser. A*, *455*, 1841–1874.

Gray, J. M. N. T., Y. C. Tai, and S. Noelle (2003), Shock waves, dead-zones and particle-free regions in rapid granular free surface flows, *J. Fluid Mech.*, *491*, 161–181.

Greve, R., and K. Hutter (1993), Motion of a granular avalanche in a convex and concave curved chute: experiments and theoretical predictions, *Philos. Trans. R. Soc. London, Ser. A*, *342*, 573–600.

Han, R., T. Shimamoto, T. Hirose, J. H. Ree, and J. Ando (2007), Ultra-low friction of carbonate faults caused by thermal decomposition, *Science*, *316*, 878–881.

Han, R. H., T. Hirose, and T. Shimamoto (2010), Strong velocity weakening and powder lubrication of simulated carbonate faults at seismic slip rates, *J. Geophys. Res.*, *115*, B03412, doi:10.1029/2008JB006136.

Heim, A. (1932), Bergsturz und menschenleben, *Vierteljahrsschr. Naturforsch. Ges. Zurich*, *77*, 218.

Hirose, T., and T. Shimamoto (2005), Growth of molten zone as a mechanism of slip weakening of simulated faults in gabbro during frictional melting, *J. Geophys. Res.*, *110*, B05202, doi:10.1029/2004JB003207.

Hsu, S. K. (2002), Imaging magnetic sources using Euler's equation, *Geophys. Prospect.*, *50*, 15–25.

Hsu, S. K., D. Coppens, and C. T. Shyu (1998), Depth to magnetic source using the generalized analytic signal technique, *Geophysics*, *63*, 1947–1957.

Hui, W. H. (2007), The unified coordinate system in computational fluid dynamics, *Commun. Comput. Phys.*, *2*(4), 577–610.

Hui, W. H., and S. Koudriakov (2002), Computation of the shallow water equations using the unifed coordinates, *SIAM J. Sci. Comput.*, *23*(5), 1615–1654.

Hungr, O., and S. McDougall (2009), Two numerical models for landslide dynamic analysis, *Comput. Geosci.*, *35*, 978–992.

Iverson, R. M. (2005), Regulation of landslide motion by dilatancy and pore pressure feedback, *J. Geophys. Res.*, *110*, F02015, doi:10.1029/2004JF000268.

Iverson, R. M., and R. P. Denlinger (2001), Flow of variably fluidized granular masses across three-dimensional terrain: 1. Coulomb mixture theory, *J. Geophys. Res.*, *106*, 537–552, doi:10.1029/2000JB900329.

Iverson, R. M., M. Logan, and R. P. Denlinger (2004), Granular avalanches across irregular three-dimensional terrain: 2. Experimental tests, *J. Geophys. Res.*, *109*, F01015, doi:10.1029/2003JF000084.

Jiang, G.-S., and E. Tadmor (1997), Non-oscillatory central schemes for multidimensional hyperbolic conservation laws, *SIAM J. Sci. Comput.*, *19*(6), 1892–1917.

Kelfoun, K., and T. H. Druitt (2005), Numerical modeling of the emplacement of Socompa rock avalanche, Chile, *J. Geophys. Res.*, *110*, B12202, doi:10.1029/2005JB003758.

Kitajima, H., J. S. Chester, F. M. Chester, and T. Shimamoto (2010), High-speed friction of disaggregated ultracataclasite in rotary shear:

Characterization of frictional heating, mechanical behavior, and microstructure evolution, *J. Geophys. Res.*, *115*, B08408, doi:10.1029/2009JB007038.

Koch, T., R. Greve, and K. Hutter (1994), Unconfined flow of granular avalanches along a partly curved surface. II. Experiments and numerical computations, *Proc. R. Soc. London, Ser. A*, *445*, 415–435.

Kuo, C. Y., Y. C. Tai, F. Bouchut, A. Mangeney, M. Pelanti, R. F. Chen, and K. J. Chang (2009), Simulation of Tsaoling landslide, Taiwan, based on Saint Venant equations over general topography, *Eng. Geol.*, *104*, 181–189.

Legros, F. (2002), The mobility of long-runout landslides, *Eng. Geol.*, *63*, 301–331.

Li, M. H., R. T. Sung, J. J. Dong, C. T. Lee, and C. C. Chen (2010), The formation and breaching of a short-lived landslide dam at Hsiaolin Village, Taiwan—Part II: Simulation of debris flow with landslide dam breach, *Eng. Geol.*, doi:10.1016/j.enggeo.2011.05.002, in press.

Lin, C. H., H. Kumagai, M. Ando, and T. C. Shin (2010), Detection of landslides and submarine slumps using broadband seismic networks, *Geophys. Res. Lett.*, *37*, L22309, doi:10.1029/2010GL044685.

Liu, Y., C.-W. Shu, E. Tadmor, and M. Zhang (2007), Non-oscillatory hierarchical reconstruction for central and finite volume schemes, *Commun. Comput. Phys.*, *2*, 933–963.

Luca, I., Y. C. Tai, and C. Y. Kuo (2009a), Non-cartesian, topography based avalanche equations and approximations of gravity driven flows of ideal and viscous fluids, *Math. Models Methods Appl. Sci.*, *19*, 127–171.

Luca, I., K. Hutter, Y. C. Tai, and C. Y. Kuo (2009b), A hierarchy of avalanche models on arbitrary topography, *Acta Mech.*, *205*, 121–149.

Luca, I., K. Hutter, Y. C. Tai, and C. Y. Kuo (2009c), A hierarchy of avalanche models on arbitrary topography, *Acta Mech.*, *205*, 121–149.

McDougall, S., and O. Hungr (2004), A model for the analysis of rapid landslide motion across three-dimensional terrain, *Can. Geotech. J.*, *41*, 1084–1097.

Miyamoto, Y., T. Shimamoto, T. Togo, J. J. Dong, and C. T. Lee (2009), Dynamic weakening of shale and bedding-parallel fault gouge as a possible mechanism for Tsaoling landslide induced by 1999 Chi-Chi earthquake, paper presented at the Next Generation of Research on Earthquake-induced Landslides: An International Conference in Commemoration of 10th Anniversary of the Chi-Chi Earthquake, Natl. Cent. Univ., Jhongli, Taiwan.

Mizoguchi, K., T. Hirose, T. Shimamoto, and E. Fukuyama (2007), Reconstruction of seismic faulting by high-velocity friction experiments: An example of the 1995 Kobe earthquake, *Geophys. Res. Lett.*, *34*, L01308, doi:10.1029/2006GL027931.

Nelder, J. A., and R. Mead (1965), A simplex method for function minimization, *Comput. J.*, *7*, 308–315.

Pitman, E. B., and L. Le (2005), A two-fluid model for avalanche and debris flows, *Philos. Trans. R. Soc. A*, *363*, 1573–1601.

Pudasaini, S. P., and K. Hutter (2003), Rapid shear flows of dry granular massis down curved and twisted channels, *J. Fluid Mech.*, *495*, 193–208.

Pudasaini, S. P., and K. Hutter (2007), *Avalanche Dynamics: Dynamics of Rapid Flows of Dense Granular Avalanches*, Springer, Berlin.

Pudasaini, S. P., Y. Wang, and K. Hutter (2005a), Rapid motions of free-surface avalanches down curved and twisted channels and their numerical simulations, *Philos. Trans. R. Soc. A*, *363*, 1551–1571.

Pudasaini, S. P., S.-S. Hsiau, Y. Wang, and K. Hutter (2005b), Velocity measurements in dry granular avalanches using particle image velocimetry technique and comparison with theoretical predictions, *Phys. Fluids*, *17*, 093301, doi:10.1063/1.2007487.

Rericha, E. C., C. Bizon, M. D. Shattuck, and H. L. Swinney (2002), Shocks in supersonic sand, *Phys. Rev. Lett.*, *88*(1), 014302, doi:10.1103/PhysRevLett.88.014302.

Savage, S. B., and K. Hutter (1991), The dynamics of granular material from initiation to runout. Part I: Analysis, *Acta Mech.*, *86*, 201–223.

Scheidegger, A. E. (1973), On the prediction of the reach and velocity of catastrophic landslides, *Rock Mech.*, *5*, 231–236.

Schneider, D., P. Bartelt, J. Caplan-Auerbach, M. Christen, C. Huggel, and B. W. McArdell (2010), Insights into rock-ice avalanche dynamics by combined analysis of seismic recordings and a numerical avalanche model, *J. Geophys. Res.*, *115*, F04026, doi:10.1029/2010JF001734.

Stark, C. P., G. Ekstrom, C. Lin, R. Rau, and W. L. R. Chen (2010), Triggering and frictional sliding of large landslides during typhoon Morakot constrained by seismic wave inversion and modeling, *Eos Trans. AGU*, *91*, West Pac. Geophys. Meet. Suppl., Abstract U33D-04.

Staron, L., and E. Lajeunesse (2009), Understanding how volume affects the mobility of dry debris flows, *Geophys. Res. Lett.*, *36*, L12402, doi:10.1029/2009GL038229.

Tai, Y. C., and C. Y. Kuo (2008), A new model of granular flows over general topography with erosion and deposition, *Acta Mech.*, *199*, 71–96.

Tai, Y. C., and Y. C. Lin (2008), A focused view of the behavior of granular flows down a confined inclined chute into the horizontal runout zone, *Phys. Fluid*, *20*, 123302, doi:10.1063/1.3033490.

Tai, Y. C., S. Noelle, J. M. N. T. Gray, and K. Hutter (2002), Shock-capturing and front tracking methods for granular avalanches, *J. Comput. Phys.*, *175*, 269–301.

Togo, T., T. Shimamoto, S. Ma, and T. Hirose (2009), High-velocity friction experiments on the longmenshan fault gouge towards the understanding of dynamic rupture propagation of the 2008 Wenchuan earthquake, paper presented at the Next Generation of Research on Earthquake-induced Landslides: An International Conference in Commemoration of 10th Anniversary of the Chi-Chi Earthquake, Natl. Cent. Univ., Jhongli, Taiwan.

Tsou, C. Y., Z. Y. Feng, and M. Chigira (2011), Catastrophic landslide induced by Typhoon Morakot, Shiaolin, Taiwan, *Geomorphology*, *127*, 166–178.

Vardoulakis, I. (2002a), Dynamic thermo-poro-mechanical analysis of catastrophic landslides, *Geotechnique*, *52*, 157–171.

Vardoulakis, I. (2002b), Steady shear and thermal run-away in clayey gouges, *Int. J. Solids Struct.*, *39*, 3831–3844.

Voellmy, A. (1955), Uber die zerstrorungskraft von lawinen, *Schweiz. Bauztg.*, *73*, 212–285.

Wang, Y., S. P. Pudasaini, and K. Hutter (2004), The Savage-Hutter theory: A system of partial differential equations for avalanche flows of snow, debris and mud, *J. Appl. Math. Mech.*, *84*, 507–527.

Wieland, M., J. M. N. T. Gray, and K. Hutter (1999), Channelized free-surface flow of cohesionless granular avalanches in a chute with shallow lateral curvature, *J. Fluid Mech.*, *392*, 73–100.

Wu, J. H., and C. H. Chen (2011), Application of DDA to simulate characteristics of Tsaolin landslide, *Comput. Geotech.*, *38*, 741–750.

Yano, K., T. Shimamoto, K. Oohashi, J. J. Dong, and C. T. Lee (2009), Ultra-low friction of shale and clayey fault gouge at high velocities: implication for Jiufengershan landslide induced by 1999 Chi-Chi earthquake, paper presented at the Next Generation of Research on Earthquake-induced Landslides: An International Conference in Commemoration of 10th Anniversary of the Chi-Chi Earthquake, Natl. Cent. Univ., Jhongli, Taiwan.

K. J. Chang and A. Y. Siau, Department of Civil Engineering, National Taipei University of Technology, No. 1 Sec. 3 Chung-Hsiao E. Rd., Taipei 106, Taiwan.

C. C. Chen, Graduate Institute of Geophysics and Department of Earth Sciences, National Central University, 300 Jung-da Rd., Jhongli 320, Taiwan.

J. J. Dong and C. T. Lee, Graduate Institute of Applied Geology, National Central University, 300 Jung-da Rd., Jhongli 320, Taiwan.

R. H. Han, Geologic Environment Division, Korea Institute of Geoscience and Mineral Resources, 92 Gwahang-no Yuseong-gu, Daejeon 305-350, South Korea.

C. Y. Kuo, Research Center for Applied Sciences, Academia Sinica, 128 2nd Academia Rd., Taipei 115, Taiwan. (cykuo06@gate.sinica.edu.tw)

T. Shimamoto, State Key Laboratory of Earthquake Dynamics, Institute of Geology, China Earthquake Administration, PO Box 9803, Beijing 100029, China.

Y. C. Tai, Department of Hydraulic and Ocean Engineering, National Cheng Kung University, Tainan 701, Taiwan.